Validation of EHL contact predictions under time varying load

C H Venner* and **Y H Wijnant**
Faculty of Engineering Technology, University of Twente, Enschede, The Netherlands

Abstract: In this paper, it is investigated how accurately current models predict the response of an elasto-hydrodynamic lubrication contact to time varying load conditions. For two patterns of time varying load, under conditions of pure rolling, the results obtained experimentally on a ball on disk interferometry apparatus by Sakamoto *et al.* (Behaviour of point contact EHL films under pulsating loads. Proceedings of the 30th Leeds–Lyon Symposium on Tribology, Elseviers Tribology Series, in press) are compared with the results of numerical simulations using the dynamic contact model of Wijnant (Contact dynamics in the field of elastohydrodynamic lubrication. PhD Thesis, University of Twente, Enschede, The Netherlands, 1998 ISBN 90-36512239), Wijnant and Venner (Contact dynamics in starved elastohydrodynamic lubrication. Proceedings of the 25th Leeds-Lyon Symposium on Tribology, Elsevier Tribology Series, Vol. 36, pp. 705–716.) The observed film changes are explained and related to the piezoviscous behaviour of the lubricant. Results for two different viscosity pressure relations are presented. It is shown that the details of the viscosity pressure relation have little effect on the local phenomena observed. The agreement between experimental and theoretical results is excellent in terms of the location and width of induced film thickness changes. The accuracy of the amplitude of the predicted changes is less. A more accurate amplitude prediction requires more precise knowledge of the dynamic parameters, which describe the load system used in the experiments.

Keywords: elasto-hydrodynamic lubrication, validation, contact dynamics

1 INTRODUCTION

General trends in design towards weight reduction and increased efficiency lead to increasingly severe conditions under which elasto-hydrodynamically lubricated (EHL) contacts have to operate reliably, e.g. higher loads, higher temperatures, and consequently smaller lubricant film thicknesses. Under these conditions, the effects of surface roughness or microgeometry on the operation of the contact increases. In fact, microgeometry is gradually becoming a design parameter. Detailed analysis and prediction of the effects of microgeometry on contact performance by definition imply studying a time-dependent problems as the roughness moves through the contact. Another reason to take into account time-dependent effects when studying EHL problems is when the operating conditions vary with time. This is the case for contacts operating under oscillatory conditions as in cam-follower mechanisms or roller bearings, in which a rolling element passes through a cycle of loading and unloading. In most other cases, at least during part of the operation, i.e. at start up and shut down, the operating conditions vary in time. When the time in which the conditions vary is large, compared with time a fluid particle spends in the contact, the effect on the film thickness will mainly be a change of the nominal level in time. However, when the conditions change more rapidly, local changes in the film thickness will also occur as a result of propagation phenomena, in which magnitude can easily be as large as those induced by surface roughness. Naturally, in real problems, both the effects of the time variation of the conditions and the surface roughness can occur at the same time and interact.

Corresponding author: Faculty of Engineering Technology, University of Twente, PO Box 217, 7500 AE Enschede, The Netherlands.

JET59 © IMechE 2005

Proc. IMechE Vol. 219 Part J: J. Engineering Tribology

Therefore, when the conditions under which a contact operates become more extreme, e.g. when the film is smaller, it is even more important that time-dependent effects are taken into account. Finally, environmental demands are towards increasingly silent machines with low vibration levels. This obviously requires control of vibrations in the bearings. To be able to predict bearing vibrations also, the dynamic behaviour of a single EHL contact must be well understood. Therefore for many reasons a detailed understanding of the time-dependent phenomena occurring in EHL contacts is needed and this understanding should be translated into simple rules for actual design.

In the past decades, the experimental and theoretical tools to study the behaviour of EHL contacts have been developed to a very high level. Optical interferometry, introduced by Foord *et al.* [1], combined with high speed cameras makes it possible to measure time-dependent phenomena [2]. When used in combination with a spacer layer, this technique even allows film thicknesses to be measured accurately down to a few nanometers, [3–5].

On the theoretical side, due to stable and efficient algorithms aided by faster computers, the detailed study of transient phenomena has also become possible. A major step forward in this respect has been the introduction and further development of multigrid/multilevel techniques [6].

As a result, detailed validations of the predictions of EHL models for single contact behaviour are possible. Such validations are of the utmost importance to identify the limitations of the models and to stimulate the new model development. In this paper, the accuracy of the model introduced by Wijnant *et al.* [7, 8] is investigated. In reference [9], it has been shown that, qualitatively, the agreement between model predictions and experimental results was quite good but, because in the experimental setup the verification of the fringe order was lost after the sudden impact, a quantitative comparison could not be done. Recently, Sakamoto *et al.* [10] presented results of the film thickness as a function of time for two experiments in which the load was varied in time under conditions of pure rolling. In this paper, these experimental results are compared with the results of numerical simulations. The observed film changes are explained and related to the piezoviscous behaviour of the lubricant. Also the effect of the dynamic behaviour of the contact on the results is investigated.

2 THEORY

The model used is a standard EHL circular contact model with the force balance equation replaced by

an equation of motion [7, 8]. The dimensionless Reynolds equation is given by

$$\frac{\partial}{\partial X}\left(\epsilon\frac{\partial P}{\partial X}\right) + \frac{\partial}{\partial Y}\left(\epsilon\frac{\partial P}{\partial Y}\right) - \frac{\partial(\bar{\rho}H)}{\partial X} - \frac{\partial(\bar{\rho}H)}{\partial T} = 0 \qquad (1)$$

where

$$\epsilon = \frac{\bar{\rho}H^3}{\eta\bar{\lambda}} \quad \text{with}\bar{\lambda} = \frac{6u_s\eta_0 a}{c^2 p_h}$$

The boundary conditions are $P(X_a, Y) = P(X_b, Y) = (X_a, Y) = P(X_b, Y) = P(X, Y_a) = P(X, Y_b) = 0$, where X_a, X_b, Y_a, and Y_b denote the boundaries of the domain. The solution should satisfy the cavitation condition; $P(X, Y, T) \geqslant 0$.

The compressibility of the lubricant is modelled according to the Dowson and Higginson equation [11]. The viscosity–pressure relation of Roelands [12] has been used. In addition, the Yasutomi [13] free volume equation has been used.

The dimensionless film thickness equation is

$$H(X, Y, T) = -\Delta(T) + \frac{X^2}{2} + \frac{Y^2}{2}$$
$$+ \frac{2}{\pi^2} \int\!\!\int \frac{P(X', Y', T)\mathrm{d}X'\mathrm{d}Y'}{\sqrt{(X - X')^2 + (Y - Y')^2}} \qquad (2)$$

The last term in equation (2) denotes the combined elastic deformation of the two surfaces. $\Delta(T)$ represents the dimensionless mutual approach of two remote points in the solids and is determined by the equation of motion

$$\frac{1}{\Omega^2}\frac{\mathrm{d}^2\Delta}{\mathrm{d}T^2} + \frac{3}{2\pi}\int\!\!\int_s P(X,Y,T)\mathrm{d}X\mathrm{d}Y = \mathcal{F}(T) \qquad (3)$$

in equation (3) Ω is the dimensionless natural frequency representing the inertia effects see (Notation). For $\Omega \to \infty$, equation (3) reduces to the usual force balance condition. Note that Ω is defined based on the nominal load F_N. For this nominal load, in fact, any value can be taken. It is of importance only for the scaling. In this study, the first value of the load in the load cycle will be taken as nominal load. The actual load of the contact is $F(T)$. $\mathcal{F}(T)$ gives the variation of this load, scaled upon the nominal load: $\mathcal{F}(T) = F(T)/F_N$.

3 NUMERICAL SOLUTION

The equations were discretized with second-order accuracy on a uniform grid. For the third and fourth term in equation (1), denoted by the wedge and squeeze term, respectively, a narrow upstream second-order discretization was used [7, 14]. The equation of motion was discretized using the

Newmark scheme; see references see [7, 8], in order to minimize numerical dissipation. The discrete equations (at each timestep) were solved with multigrid/multilevel techniques [6]. The calculational domain ($X \in [-6.75; 3.25]$, $Y \in [-5.0; 5.0]$) was covered with a uniform grid with 513×513 grid-points. The timestep was taken equal to the mesh size. The discretization error in the solutions obtained is <1 per cent, see Appendix 2.

4 RESULTS

Sakamoto et al. [10] have presented results obtained with a ball on disk optical interferometry apparatus for two situations: an oscillatory load and an impact load. In this paper, the results obtained with the theoretical model for these situations will be presented and compared with the experimental results.

The load patterns are illustrated in Fig. 1. For the first case the load is increased from 4.3 to 56 N in ∼50 ms, kept at this level for 200 ms and subsequently

Fig. 1 Measured force variation with time for oscillatory load (top) and impact load (bottom) considered in the experiments of Sakamoto et al. [10]

decreased again. This case will be referred to as the oscillatory load case. For the second case, the load is increased from 3.9 to 65 N in 15 ms after which a damped oscillation is observed. This will be referred to as the impact load case.

The oil used in the experiment was a Bright Stock mineral oil. The measured viscosity and pressure viscosity coefficients, as given by Sakamoto et al. [10] are listed in Table 1. The values of the different parameters in the Yasutomi free volume equation obtained from measurements are given in Table 1.

The values of the different material and lubricant parameters and the rolling speed are given in Table 2. Also, the values of some commonly used dimensionless parameters are given. Finally, the range of variation of the load-dependent parameters such as the Hertzian pressure, the Hertzian contact radius, and the dimensionless parameters in which the load appears are indicated in Table 3.

The results will be presented in dimensional quantities to facilitate direct comparison with the experimental results. First, for reference, in Fig. 2, the computed centreline film thickness profiles are shown for a steady state load of $F = 4\,\text{N}$ and $F = 60\,\text{N}$ obtained using the Roelands equation. Also, the results obtained when the Yasutomi equation is used for temperatures $\bar{T} = 20$, 22, and 25°C are shown. The computed steady state central film thickness for $F = 4\,\text{N}$ is 172 nm when using the Roelands equation. When the Yasutomi equation is used, the central film thickness values are 237, 210, and 178 nm for $\bar{T} = 20$, 22, and 25°C, respectively. The computed steady state central film thickness for $F = 60\,\text{N}$ is 138 nm when the Roelands equation is used and 196, 172, and 142 nm when the Yasutomi equation is used with $\bar{T} = 20$, 22, and 25°C, respectively. The central film thickness values obtained experimentally for these loads are 170 and 150 nm. The differences between the experimental and theoretical values are mainly a proof of the sensitivity of the film thickness level to the inlet viscosity and its strong dependence on the temperature. The exact
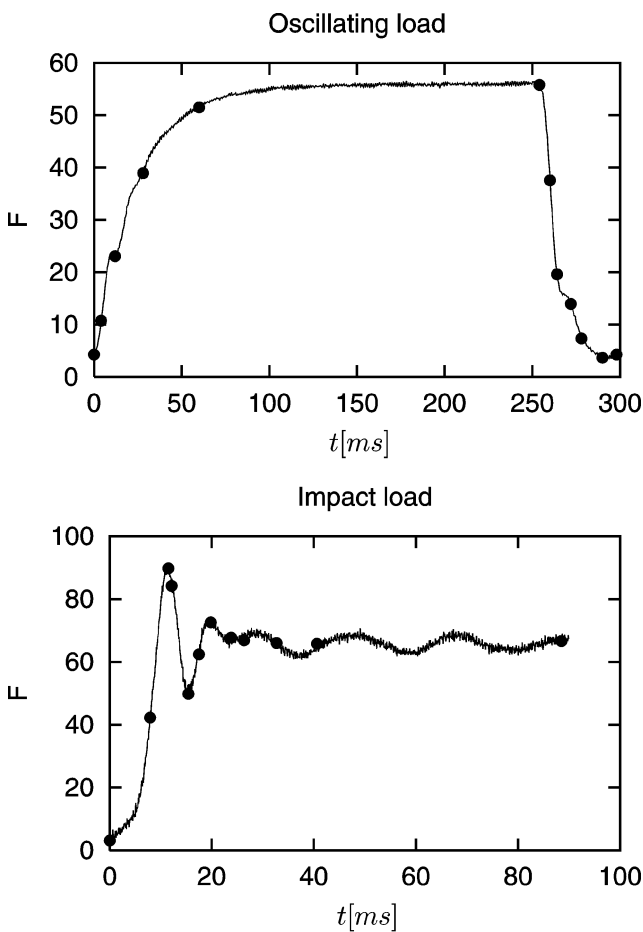
Table 1 Parameters in viscosity pressure equation of Roelands and of Yasutomi used in the calculations

Parameter	Value	Dimension
η_0	1.22	(Pa s)
α	2.248×10^{-8}	(Pa^{-1})
Z	0.45	
η_g	1.000×10^7	
T_{g0}	-4.794×10^1	(°C)
A_1	3.840×10^2	(°C)
A_2	2.904×10^{-10}	(Pa^{-1})
B_1	1.541×10^{-1}	
B_2	4.615×10^{-8}	(Pa^{-1})
C_1	1.088×10^1	
C_2	3.906×10^1	(°C)

Table 2 Parameters and dimensionless parameters of the contact on the ball on disc apparatus

Parameters	Value	Dimension
F	$4 \leqslant F \leqslant 60$	(N)
R_x	12.52×10^{-3}	(m)
E'(sapphire-steel)	1.17×10^{11}	(Pa)
$\bar{u}$	0.012	(ms^{-1})
Dimensionless parameters		
U	1.0×10^{-11}	
G	2630	
L	5.56	

temperature at which the experiments were carried out is not known.

The results of the complete dynamic simulations for the two time varying load patterns are presented in the sections 4.1 and 4.2 subsequently. In the simulations, the equation of motion (3) was used with $\Omega = 5.13$. The exact value of Ω to be taken is not known because the effective mass of the system is not known. For $\Omega = 5.13$, the results are still quite close to those obtained assuming force balance. In section 5, the influence of Ω on the results is illustrated in detail.

4.1 Oscillating load

A characteristic time appropriate for the contact is the time needed for a fluid particle to travel from the inlet of the contact to the outlet; $t_c = 2a/\bar{u}$. Here, $0.014 \leqslant t_c \leqslant 0.036$ s which is relatively short when compared with the period of oscillation of the load, so it is sufficient to restrict the simulation to a single load cycle as shown in Fig. 1.

In Figs 3 and 4, results obtained for the oscillating load case are presented. In these figures, the interferogram of the film thickness as measured, the interferogram of the computed film thickness (based on the Roelands equation), and a graph of the film thickness at the centreline of the contact at different times in the cycle are shown. The times taken are indicated with black dots in Fig. 1. Note that the colour and spatial scaling of the experimental and theoretical interferograms is not exactly the same. In the centreline graphs, the results obtained using the Roelands equation and those obtained

Table 3 Values of Hertzian contact parameters and the load dependent dimensionless parameters for the reference cases $F = 4$ and 60 N

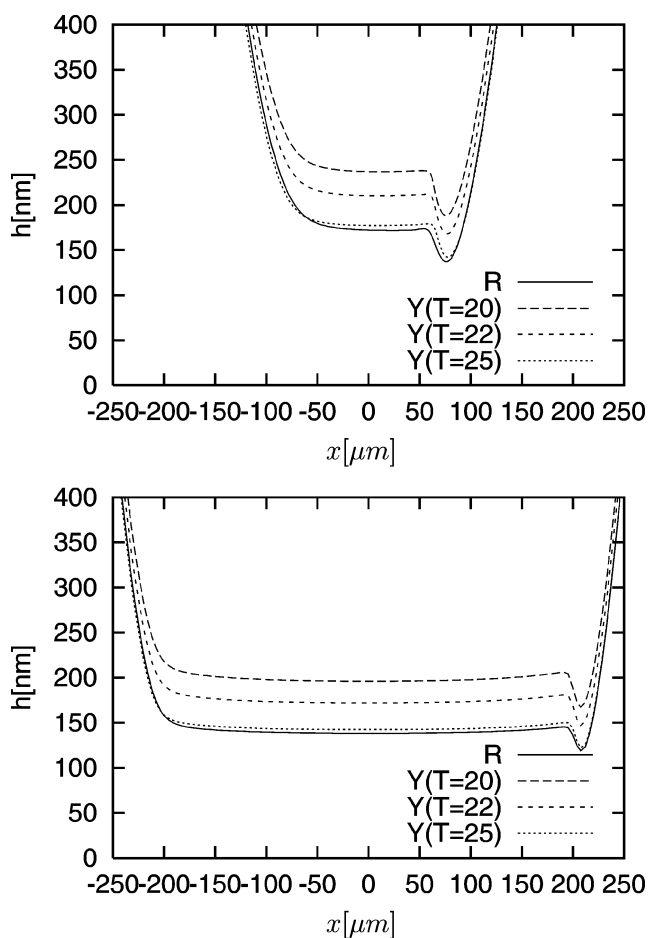| Parameter	$F = 4$ N	$F = 60$ N	unit
a	8.63×10^{-5}	2.13×10^{-4}	[m]
p_h	2.57×10^8	6.33×10^8	[Pa]
W	2.18×10^{-7}	3.27×10^{-6}	
M	23.07	345.87	

Fig. 2 Computed film thickness at the centerline $y = 0$ as a function of x for loads $F = 4$ and $F = 60$ N obtained when using the Roelands (R) viscosity pressure equation, and the Yasutomi (Y) viscosity pressure equation with $\bar{T} = 20$, 22, and 25°C, respectively

with the Yasutomi equation for temperatures $\bar{T} = 20$, 22, and 25°C are shown. The markers in these graphs indicate the film thickness values at different positions x from the measurements.

As expected, the response of the contact to the increase of the load is a transition from low load small Hertzian contact region to high load large contact region. The film thickness decreases too but as is well known, the film thickness is not so very sensitive to the load. The transition takes place via local film thickness changes formed in the outer region of the contact. The effects observed are essentially the same as those observed for a line contact by Hooke in reference [15] and for a point contact by Wijnant in reference [7]. They can be explained by the exponential viscosity pressure dependence and the resulting shear flow dominance.

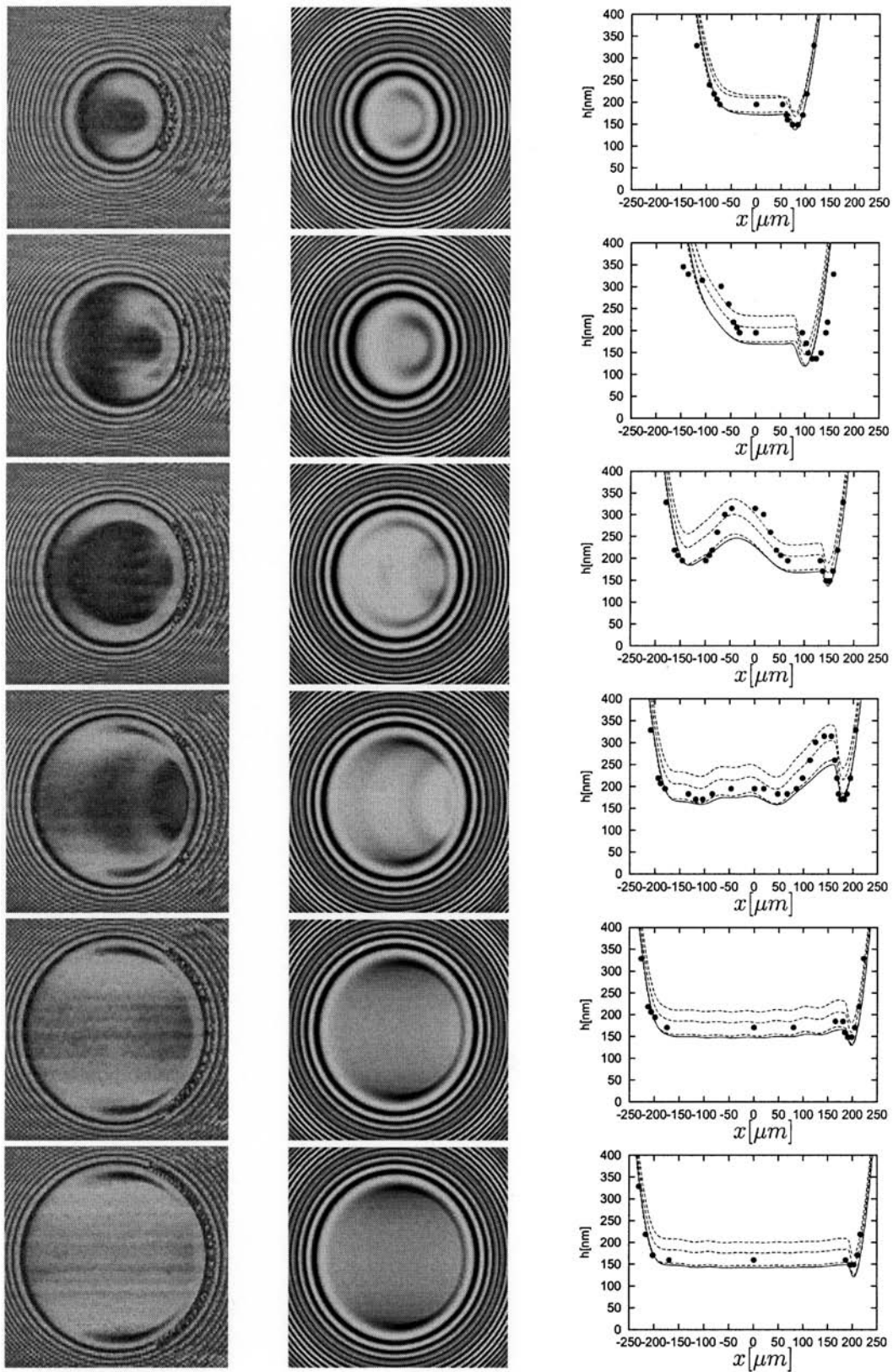Owing to the high viscosity in the centre, the film thickness in the central region is very stiff when

Fig. 3 Interferograms of measured (left) and computed (centre) film thickness and film thickness h at the centreline $y = 0$ (right), at $t = 0, 4, 12, 28, 60$ and 256 ms (top to bottom). The dots in the centreline film thickness graphs indicated measured values. The curves are the calculation results obtained using Roelands pressure viscosity equation and the Yasotomi equation for $\bar{T} = 20, 22,$ and $25°C$, respectively (Fig. 2). Oscillatory load case, $\Omega = 5.13$
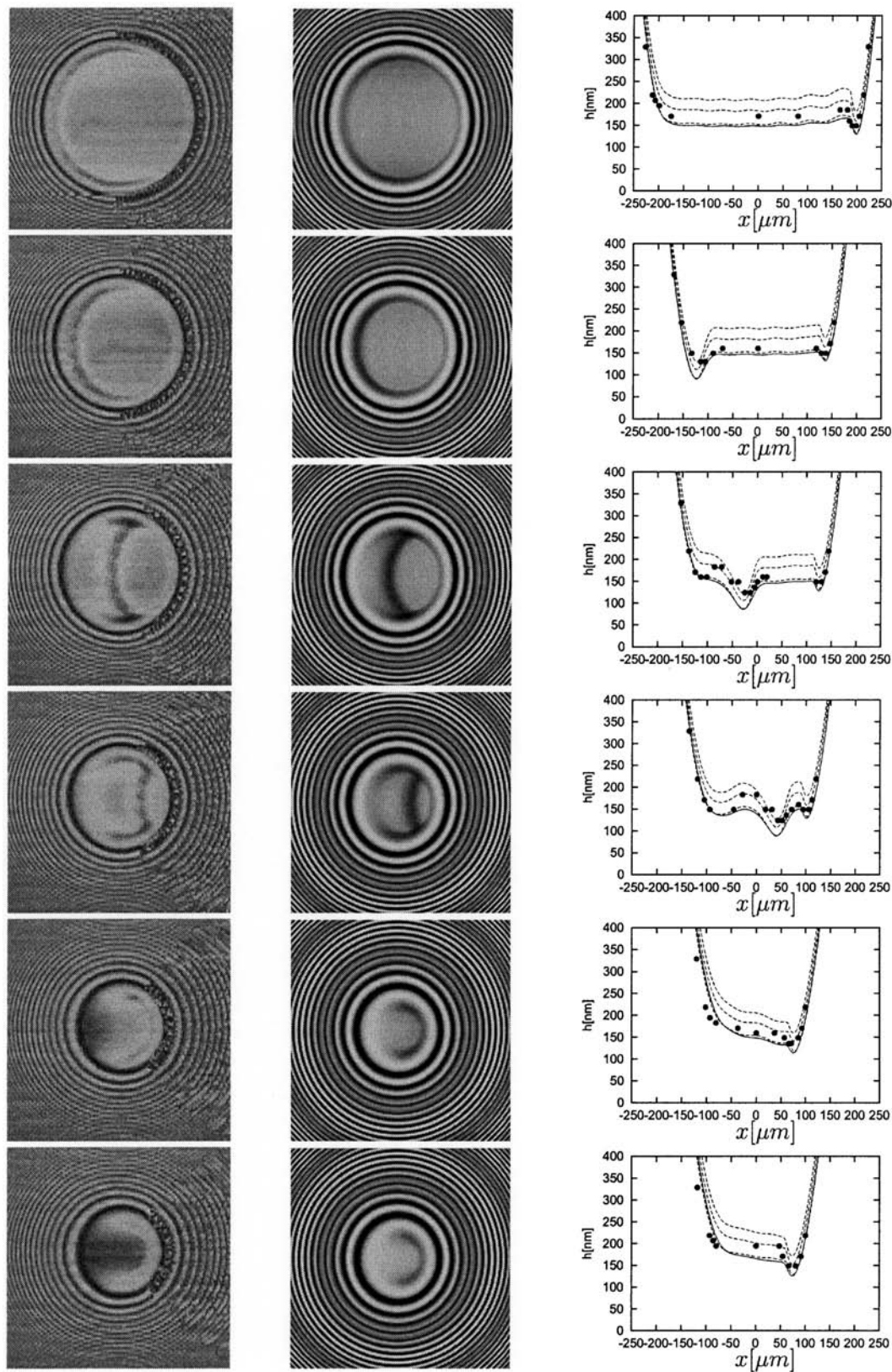
Fig. 4 Interferograms of measured (left) and computed (centre) film thickness and film thickness h at the centreline $y = 0$ (right), at $t = 260$, 264, 272, 278, 290, and 298 ms (top to bottom). The dots in the centreline film thickness graphs indicate measured values. The curves are the calculation results obtained using the Roelands pressure viscosity equation and the Yasotomi equation for $\bar{T} = 20$, 22, and 25°C, respectively. (Fig. 2). Oscillatory load case, $\Omega = 5.13$

compared with the film thickness in the region immediately around it. Therefore, the only way for the contact to accommodate an increase in the load is, initially, by means of a decrease in the film thickness in the area surrounding the contact where the viscosity is lower.

The reduction of the film thickness leads to higher pressures and a higher viscosity as a result of which shear flow starts to dominate in this region also. Also, in the inlet to the Hertzian contact region, it leads to a larger effective entrainment speed [15]. At the edge of the contact region on the centreline $y = 0$, the effective entrainment speed is increased from $\bar{u}$ to $\bar{u} + d\bar{a}/dt$ where $d\bar{a}/dt$ is the rate of increase of the Hertzian contact. As the entrainment speed in the contact region itself remains the same, this causes an accumulation of lubricant in a deep valley [15]. Subsequently, as a result of shear flow dominance, the created film thickness perturbation is carried through the contact by entrainment $h = h(x - \bar{u}t)$. When it has left the contact region, the contact settles into the steady situation associated with the higher load. Some remaining film thickness ripples can be seen which are associated with the dynamics of the contact. Their wavelength λ_x depends on the value of the inertia parameter Ω as will be explained in section 5.

From the figures, it can be seen that the theoretical results only differ in the nominal level of the film thickness which is due to the different inlet viscosities. The local effects in the film thickness profiles are virtually the same in depth and width. When comparing the theoretical results with the experimental results, it can be seen that the shape and the width of the local features and their position at the different times are quite accurately predicted except for the depth of the features. In particular, the propagated valley in the experimental result is deeper.

When the load is decreased the reverse process takes place. The contact changes from a large radius contact to a small radius contact via film changes in the outer region that are propagated. Because of the local decrease of the effective entrainment speed at the edge of the Hertzian contact on the inlet side, the inlet perturbation that is created now takes the form of a local film thickness decrease. This perturbation is subsequently propagated through the part of the central region where the shear flow dominates. After it has left the central region, the contact settles into the condition associated with the lower load, i.e. a smaller region of high viscosity, an increased film thickness level in the centre, and a smaller nearly flat film region in accordance with the smaller Hertzian contact radius.

As can be seen from the centreline film thickness graphs, the difference between the different theoretical results is again only in the nominal level of the film thickness. The local variations in time in the different solutions are identical. The agreement between the experimental and the theoretical results in terms of the width and the position of the features as a function of time is very good. However, here the propagated perturbation also in the experimental profile is more extreme as it protrudes deeper in the film than that in the theoretical results.

4.2 Impact load

The results for the impact load are presented next. In the Figs 5 and 6, interferograms of the measured film thickness and of the computed film thickness using the Roelands equation, and of the centreline film thickness graphs with the computed film thickness for several cases, and the experimental values are shown. The times in the load cycle to which the results apply are indicated in Fig. 1.

In the figures, it can be seen that the response to the increase of the load is the same as in the oscillating load case. A lubricant entrapment is formed in the inlet region that is propagated through the contact. However, in this case, the valley is deeper because the load increases faster. As a result, the rate of change of the contact radius in the inlet region $d\bar{a}/dt$ is larger and thereby the local increase of the entrainment speed. This causes more lubricant to be entrapped and a deeper valley. Again, the film thickness perturbation is propagated through the contact by entrainment $h = h(x - \bar{u}t)$. Finally, note that in Fig. 5, it can be seen that ahead of the propagated valley of entrapped lubricant, the entire film thickness image of the low load situation is in fact propagated out of the contact.

Because in this case the high load level is reached via a damped oscillation, the centreline film thickness graphs show the evidence of a series of inlet changes (valleys and decreases) of decreasing amplitude travelling through the contact. Each increase or decrease of the load causes a perturbation in the inlet of the contact which is then propagated through the contact. Apart from the nominal level of the film thickness, the theoretical results are all the same. Note that for this case, the agreement between the experimental and theoretical results both with respect to the location and width of the local features and with respect to their depth is very good.

5 DISCUSSION

In general, the predicted dynamic behaviour agrees quite well with the experimentally observed behaviour. This applies in particular to the location and the width of the local features occurring in the film
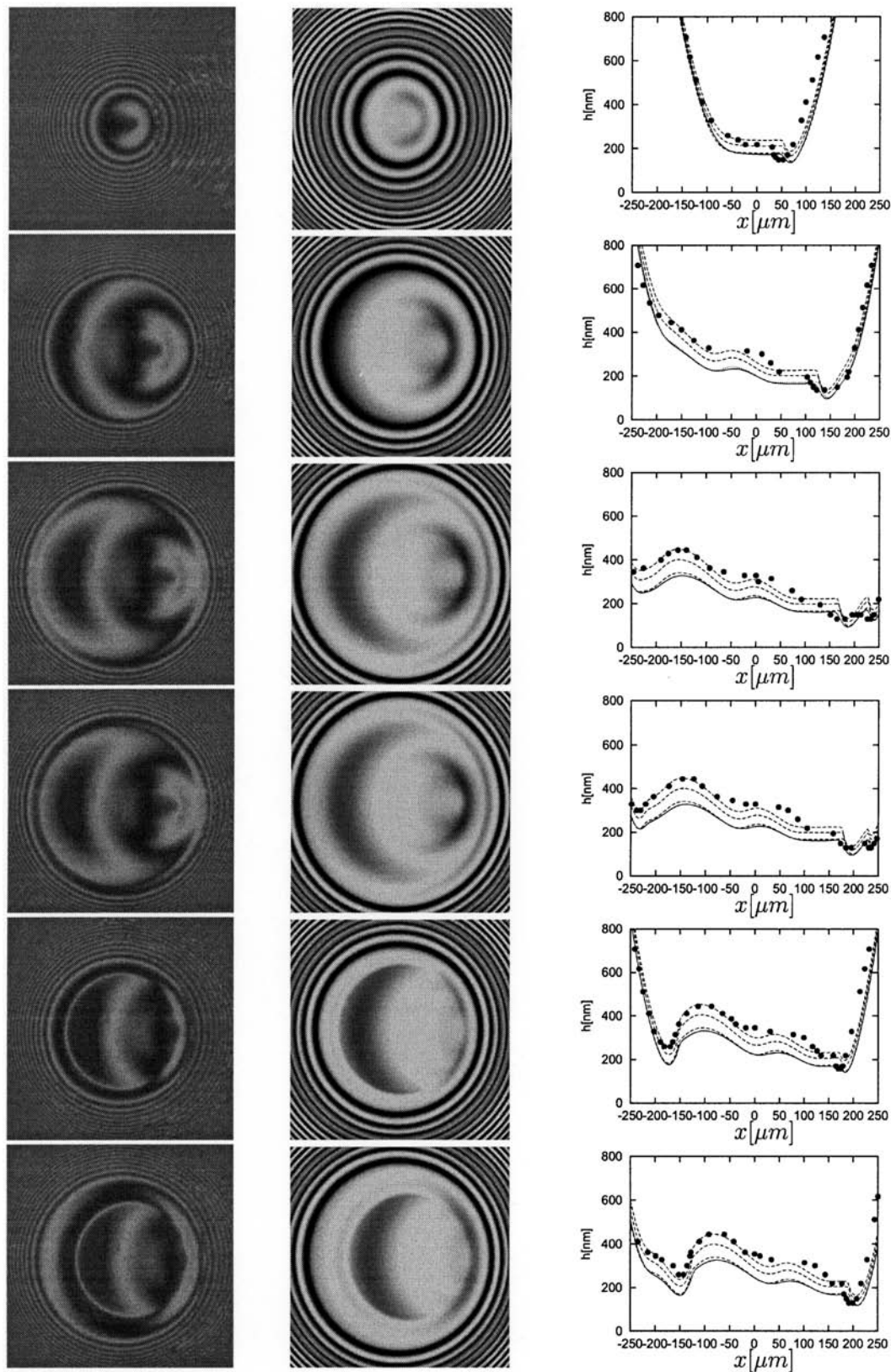
Fig. 5 Interferograms of measured (left) and computed (centre) film thickness and film thickness h at the centreline $y = 0$ (right), at $t = 0$, 8, 11.5, 12.1, 15.4, and 17.5 ms (top to bottom). The dots in the centreline film thickness graphs indicate measured values. The curves are the calculation results obtained using the Roelands pressure viscosity equation and the Yasotomi equation for $\bar{T} = 20$, 22, and 25 °C, respectively (Fig. 2). Impact load case, $\Omega = 5.13$

Fig. 6 Interferograms of measured (left) and computed (centre) film thickness and film thickness h at the centreline $y = 0$ (right), at $t = 19.8, 23.8, 26.3, 32.7, 40.6$ and 88.4 ms (top to bottom). The dots in the centreline film thickness graphs indicate measured values. The curves are the calculation results obtained using the Roelands pressure viscosity equation and the Yasotomi equation for $\bar{T} = 20, 22$, and $25°$C, respectively (Fig. 2). Impact load case, $\Omega = 5.13$
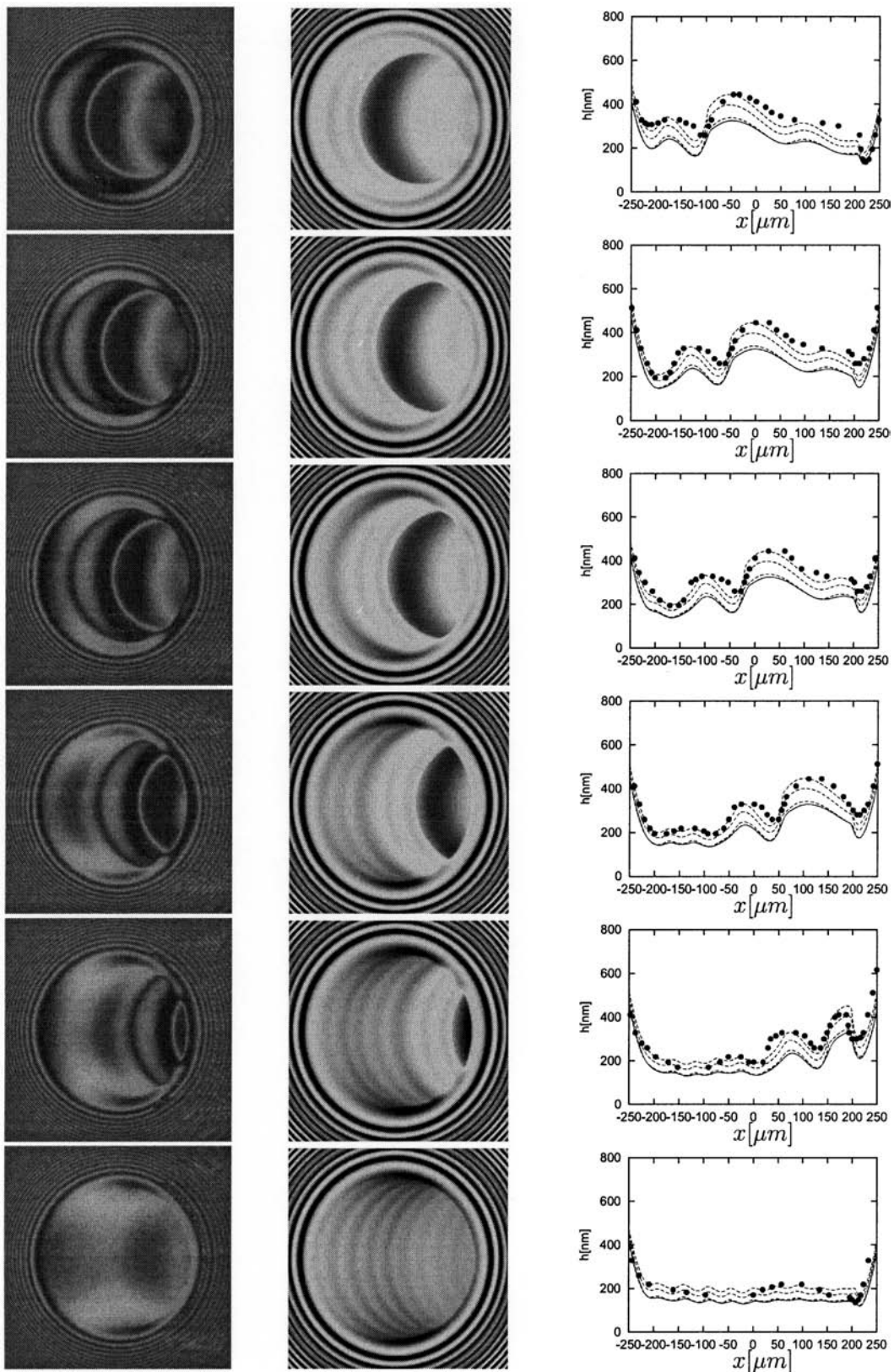
thickness in response to the load variations. For the oscillating load case, the agreement in terms of the amplitude of the propagated feature is less good. The reason for this difference is not clear. It may be due to the fact that the value of the inertia term in the experiment is larger or smaller or that the equation of motion used does not sufficiently well represent the dynamic behaviour of the load system.

The effect of the dimensionless natural frequency Ω is illustrated in Figs 7 and 8. In these figures, for each of the load variations, the centreline film thickness profiles at a given time and the time history of the central film thickness during the first part of the simulation until the load stabilizes are shown. In the centreline graphs, $h(x)$ also the measured values at different positions x are shown. By comparing the results for $\Omega > 5.13$ with those for $\Omega = \infty$, it can be seen that for the value of Ω used
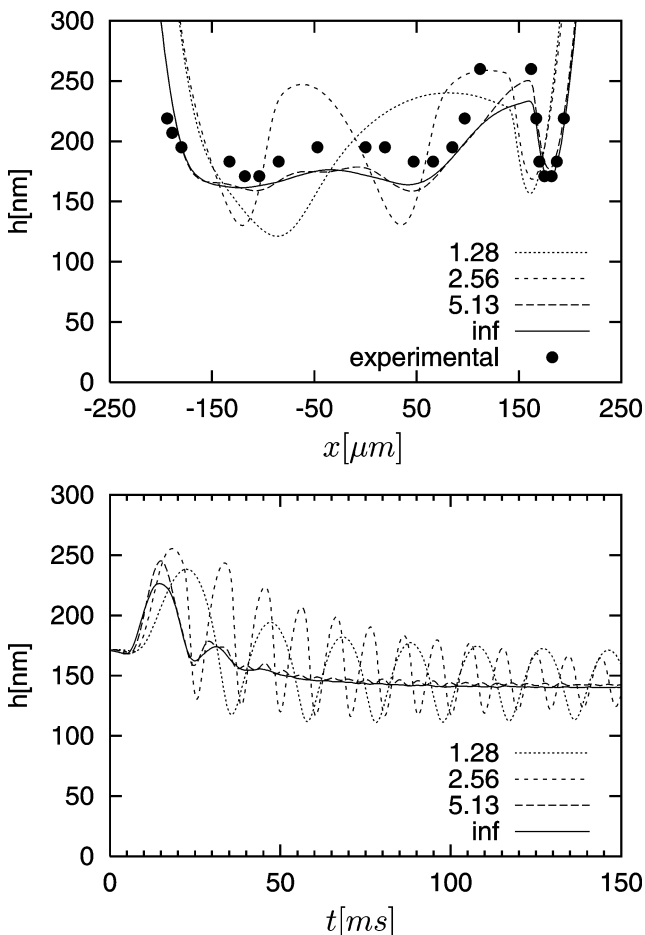

Fig. 7 Film thickness h at $y = 0$ at $t = 28$ ms (top) and central film thickness as function of time (bottom) obtained for $\Omega = 1.28$, 2.56, 5.13, and ∞ (force balance). In all cases, the Roelands pressure viscosity equation was used. Oscillating load. The dots indicate the measured film thickness values
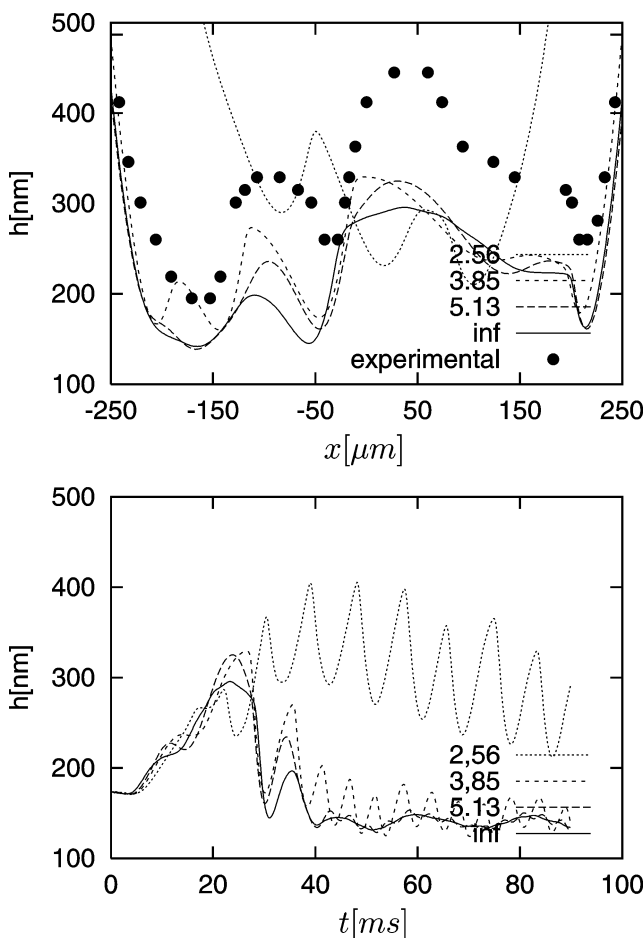

Fig. 8 Film thickness h at $y = 0$ at $t = 26.3$ ms (top) and central film thickness as function of time (bottom) obtained for $\Omega = 2.56$, 3.85, 5.13, and ∞ (force balance). In all cases, the Roelands pressure viscosity equation was used. Impact load. The dots indicate the measured film thickness values

in the simulations, the contact behaviour is nearly quasi-static with respect to the equation of motion. In the film profiles, only a minor oscillation due to inertia effects is visible, so the solution is close to the one obtained assuming force balance throughout the simulation. This also appears to agree quite well with the results obtained in the experiments in terms of the local behaviour of the film thickness.

The theoretical results for decreasing Ω illustrate the effect of decreasing inertia on the results. The oscillations in the film increase in amplitude and have an increasing effect on the film shape at a given time. This effect is strongest for the impact load case. For $\Omega = 2.56$, the inertia effects are already so strong that they affect the entire level of the film thickness over a long period in time, i.e. the film thickness does not oscillate around or near the level of the film thickness at force balance but

around a much higher value that only slowly decreases to the equilibrium value at the high load. After 80 ms, the nominal level of the film thickness is still much larger than the high load steady state value; however, as can be seen from Fig. 9 eventually it does reduce to the steady state level as should be the case.

The oscillation frequency can be predicted accurately. For a contact operating at a certain nominal load, the wavelength of the oscillations in time around its equilibrium position is given by $\lambda_t = 5.13/\bar{\Omega}(\bar{a}/\bar{u})$, see references [7, 8], where $\bar{a}$ and $\bar{\Omega}$ refer to the momentary values at this equilibrium condition. In both cases, here the condition around which the oscillation takes place is the increased load, whereas the value of Ω given as input refers to the initial load condition that was used for scaling the variables. Taking this effect into account the period of the oscillations is

$$\lambda_t = \frac{5.13}{\bar{\Omega}} = \frac{5.13}{\Omega}\left(\frac{a}{\bar{u}}\right)\left(\frac{F_{\mathrm{N}}}{F}\right)^{1/6} \tag{4}$$

where F is the value of the load around which the oscillation takes place and F_{N}, a, and $\bar{u}$ are the values for the reference conditions used in the scaling. For the oscillatory load case, the values of λ_t observed in the calculations are approximately 19.3, 9.3, and 4.6 ms for $\Omega = 1.28$, 2.56, and 5.13, respectively. The values predicted by the theory based on dry contact oscillations are 19.2, 9.6, and 4.8 ms, respectively. For the impact load case, the values of λ_t observed in the calculations are approximately: 16.5, 9.3, 6.8, 5.3, and 4.0 ms for $\Omega = 1.28$, 2.56, 3.20, 3.85 and 5.13, respectively. The values predicted by the theory based on dry contact oscillations are
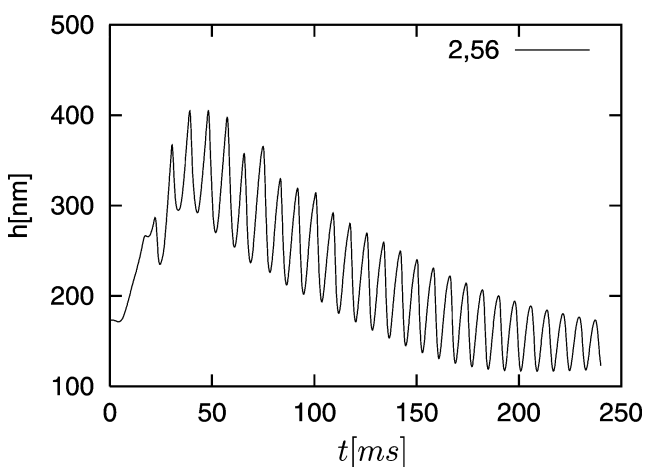
16.0., 8.0, 6.4, 5.3, and 4.0 ms, respectively. As has also been shown in earlier studies, e.g. references [7, 9, 16, 17], as far as the frequency is concerned the EHL contact behaves like a dry contact. This is a natural consequence of the extremely high viscosities leading to a very stiff film. As a result changes in the mutual separation are mainly accommodated by changes in the elastic deformation and not by changes in the film thickness.

6 CONCLUSION

By means of numerical simulations, the dynamic response of an EHL contact to time varying load was studied for two load variations for which detailed experimental results were presented by Sakamoto *et al.* [10]. The results show a very good agreement in terms of the shape and the location of the local features induced in the film thickness as a result of the time varying load. The phenomena observed can be explained from the piezoviscous behaviour of the lubricant and the resulting shear flow dominance in the central region. Results for two different viscosity pressure equations were presented and it was shown that the viscosity mainly influences the level of the film thickness and not the shape of the perturbations. With respect to the depth of the propagated changes, the agreement for the impact load case is better than that for the oscillatory load case. This might be explained by the fact that the precise dynamic behaviour of the load system used in the experiments is not known. For the impact load case, the details of this behaviour are less important as in this case inertia effects will dominate anyway. Finally, with the results of numerical simulations, it was shown how the system dynamics influences the behaviour.

Fig. 9 Central film thickness as function of time obtained for $\Omega = 2.56$. Roelands equation, impact load

REFERENCES

1 Foord, C. A., Wedeven, L. D., Westlake, F. J., and **Cameron, A.** Optical elastohydrodynamics. *Proc. Instn. Mech. Engrs,* 1969, **148**, 487–505.

2 Kaneta, M, Sakai, T., and **Nishikawa, H.** Optical interferometric observations of the bump on point contact EHL. *ASME J. Tribol.*, 1992, **114**, 779–784.

3 Johnston, G. J., Wayne, R. C., and **Spikes, H. A.,** The measurement of very thin lubricant films in concentrated contacts. *ASLE Trans.*, 1991, **34**, 187–194.

4 Cann, P. M., Spikes, H. A., and **Hutchinson, J.** The development of a spacer layer imaging method for mapping elastohydrodynamic contacts. *STLE Tribol. Trans.*, 1996, **36**(4), 915–921.

5 Choo, Glovnea, R. P., Olver, A. V., and **Spikes, H. A.** The effects of 3D model surface roughness features on lubricant film thickness in EHL Contacts. *ASME J. Tribol.*, 2003, **125**, 533–542.

6 Venner, C. H. and **Lubrecht, A. A.** *Multilevel Methods in Lubrication*, Elsevier Tribology Series, 2000, Vol. 37, ISBN 0-444-50503-2.

7 Wijnant, Y. H. Contact dynamics in the field of elastohydrodynamic lubrication. PhD Thesis, University of Twente, Enschede, The Netherlands, 1998 ISBN 90-36512239.

8 Wijnant, Y. H. and **Venner, C. H.** Contact dynamics in starved elastohydrodynamic lubrication. Proceedings of the 25th Leeds-Lyon Symposium on Tribology, Elsevier Tribology Series, Vol. 36, pp. 705–716.

9 Wijnant, Y. H., Venner, C. H., and **Larsson, R.** Effects of structural vibrations on the film thickness in an EHL circular contact. *ASME J. Tribol.*, 1999, **121**, 259–264.

10 Sakamoto M., Nishikawa, H., and **Kaneta, M.** Behaviour of point contact EHL films under pulsating loads. Proceedings of the 30th Leeds–Lyon Symposium on Tribology, Elseviers Tribology Series, in press.

11 Dowson, D. and **Higginson, G. R.** *Elastohydrodynamic Lubrication, the Fundamentals of Roller and Gear Lubrication*, (Pergamon Press, Oxford, 1966 Great Britain).

12 Roelands, C. J. A. Correlational aspects of the viscosity–temperature–pressure relationship of lubricating oils PhD Thesis, Technical University Delft, Delft, The Netherlands, 1966 (V.R.B., Groningen, The Netherlands).

13 Yasutomi, S., Bair, S., and **Winer, W. O.** An application of free volume model to lubricant rheology. *ASME J. Tribol.*, 1984, **106**, 291–303.

14 Venner, C. H. and **Morales Espejel, G. E.** Amplitude reduction of small amplitude waviness in transient elastohydrodynamically lubricated line contacts. *Proc. Instn Mech. Engrs, Part J*: J. Engineering Tribology, **213**, 487–504.

15 Hooke, C. J. Dynamic effects in EHL contacts. Proceedings of the 2002 Leeds Lyon Symposium on Tribology Elsevier Tribology Series, Vol. 41, pp. 68–78.

16 Popovici, G., Venner, C. H., and **Lugt, P. M.** Effects of load system dynamics on the film thickness in EHL contacts during start up. *ASME J. Tribol.*, 2004, **126**, 258–266.

17 Venner, C. H., Popovici, G., and **Wijnant, Y. H.** Contact dynamics of EHL contacts with time varying operating conditions. *Proceedings of the 2003 Leeds Lyon Symposium on Tribology*, Elsevier Tribology Series, Vol. 43, pp. 189–200.

APPENDIX 1

Notation

a	Hertzian contact length, $a = (3F_{N}R/E')^{1/3} = b$
$\bar{a}$	momentary Hertzian contact length, $\bar{a} = (3FR/E')^{1/3}$
c	Hertzian approach, $c = (a^2/(2R))$
$\bar{c}$	momentary Hertzian approach, $\bar{c} = (\bar{a}^2/2R)$
E	modulus of elasticity
E'	reduced modulus of elasticity, $2/E' = (1 - \nu_1^2)/E_1 + (1 - \nu_2^2)/E_2$
F	external load
F_{N}	nominal external load
$\mathcal{F}$	dimensionless force $\mathcal{F} = F/F_{N}$
G	dimensionless parameter $G = \alpha E'$
h	film thickness
H	dimensionless film thickness $H = h/c$
L	dimensionless parameter (Moes), $L = G(2U)^{1/4}$
$\bar{m}$	effective mass
M	dimensionless parameter (Moes), $M = W(2U)^{-3/4}$
p	pressure
p_{h}	maximum Hertzian pressure, $p_{h} = (3F_{N})/(2\pi a^2)$
P	dimensionless pressure $P = p/p_{h}$
R	reduced radius of curvature, $1/R = 2/R_x$
R_x	reduced radius of curvature in x, $1/R_x = 1/R_{x1} + 1/R_{x2}$
R_y	reduced radius of curvature in y, $1/R_y = 1/R_{y1} + 1/R_{y2}$
R_{x1}, R_{x2}	radius of curvature surface 1, 2 in x
R_{y1}, R_{y2}	radius of curvature surface 1, 2 in y
T	dimensionless time $T = t\bar{u}/a$
$\bar{T}$	temperature
$\mathcal{T}$	dimensionless time, $\mathcal{T} = t\sqrt{F_{N}/\bar{m}c}$
u	surface velocity
u_s	sum velocity $u_s = (u_1 + u_2)$
$\bar{u}$	entrainment velocity $\bar{u} = (u_1 + u_2)/2$
U	dimensionless parameter $U = (\eta_0\bar{u})/(E'R_x)$
W	dimensionless parameter, $W = F_{N}/(E'R_x^2)$
x, x'	coordinates in the direction of rolling
X, X'	dimensionless coordinates $X = x/a$, $X' = x'/a$
y, y'	coordinates perpendicular to x
Y, Y'	dimensionless coordinates, $Y = y/a$, $Y' = y'/a$
z	pressure viscosity index (Roelands)
α	pressure viscosity index
$\bar{\alpha}$	dimensionless parameter $\bar{\alpha} = \alpha p_{h}$, $\bar{\alpha}(L/\pi)((3M)/2)^{1/3}$
δ	mutual approach

Δ	dimensionless mutual approach, $\Delta = \delta/c$
ϵ	coefficient in Reynold's equation, $\epsilon = (\bar{\rho}H^3)/(\bar{\eta}\bar{\lambda})$
ν	Poisson ratio
$\bar{\lambda}$	dimensionless parameter, $\bar{\lambda} = 6(\eta_0 u_s a)/(c^2 p_h), ((128\pi^3)/(3M^4))^{1/3}$
λ_x	wavelength film variation in x
λ_t	period of oscillation in t
$\lambda_{\mathcal{T}}$	period of oscillation in $\mathcal{T}$, $\lambda_{\mathcal{T}} = (2\pi)/(\sqrt{3/2})$
λ_T	period of oscillation in T, $\lambda_T = \lambda_{\mathcal{T}}/\Omega$
η	viscosity
$\bar{\eta}$	dimensionless density, $\bar{\eta} = \eta/\eta_0$
Ω	nominal dimensionless natural frequency, $\Omega_N^2 = (F_N a^2)/(\bar{m}\bar{u}^2 c)$
$\bar{\Omega}$	momentary dimensionless natural frequency, $\Omega^2 = (F(t)\bar{a}^2)/(\bar{m}\bar{u}^2\bar{c})$
ρ	density
$\bar{\rho}$	dimensionless density, $\bar{\rho} = \rho/\rho_0$

Subscripts

a, b	inlet, outlet
N	nominal
0	constant, e.g. at ambient pressure
1, 2	surface 1, 2
∞	at infinity or equilibrium

APPENDIX 2

Numerical accuracy

All equations were discretized with second-order accuracy. A narrow upstream second-order combined discretization of the wedge and the squeeze term in the Reynolds equation was used, [14]. The advantage of this scheme is that it has a zero second-order truncation term for several ratios of the timestep over the mesh size. This implies a very small artificial diffusivity (cause of amplitude decay) and consequently accurate description of the characteristic behaviour $h = h(x - \bar{u}t)$ in the high viscosity region. The convergence behaviour of the solutions is illustrated in Fig. 10. In this figure, for each of the load variations the centreline film thickness profile is shown at a given time for the solutions obtained on a grid with (128×128), (256×256), and (512×512) points. In all cases, the timestep was taken equal to the mesh size. The results for the solution are obtained using the Yasutomi viscosity pressure equation with $\bar{T} = 22\,^\circ$C, but the studies show that the convergence behaviour is independent of the viscosity pressure equation. In accordance with the second-order behaviour, for sufficiently small mesh size and time
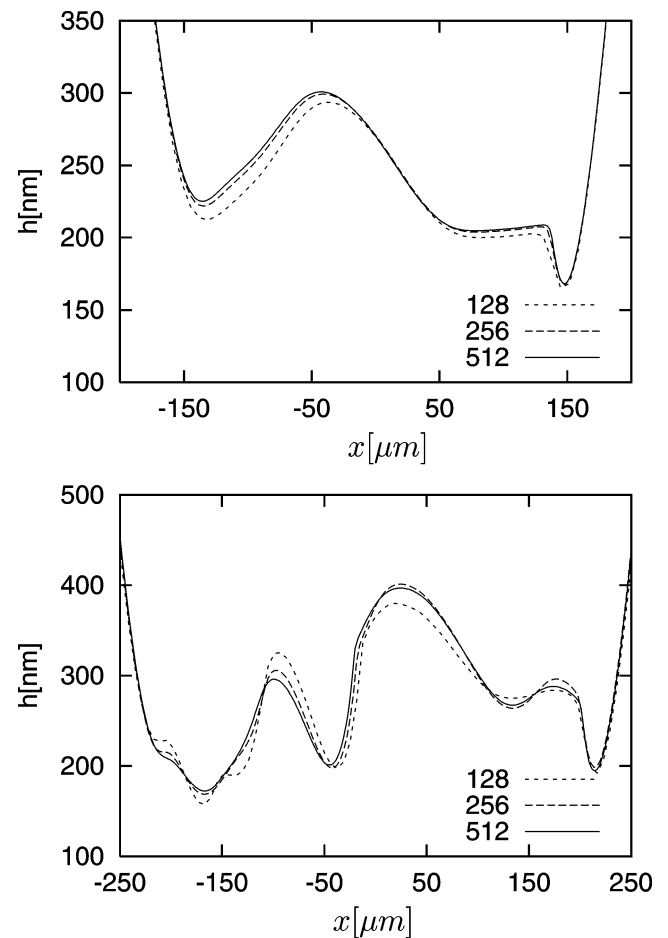

Fig. 10 Film thickness h at $y = 0$ obtained on grids with different mesh sizes and time steps at $t = 12$ ms for the oscillatory load case (top) and at $t = 26.3$ ms for the impact load case (bottom). The Roelands pressure viscosity equation was used; $\Omega = 5.13$

step, the error in space and time should decrease by a factor 4 each time the mesh size and timestep are halved. This trend can be seen in the figures, as well as in the detailed values. For example, for the oscillatory load solution at the time shown in Fig. 10 the maximum film thickness inside the contact is 293.63, 299.28, and 300.82 nm and found at position $x = -34.48$, -41.38, and $-43.10\,\mu$m. Both the change in film value and the change in the position at which the maximum occurs converge second-order. In the same way, the second-order behaviour can be seen in the solution for the impact load. The values of the local minimum in the centre of the contact at $t = 26.3$ ms are 179.94, 197.66, and 200.94 nm and its position is $x = -37.1$, -43.32, and $-44.87\,\mu$m, respectively, for the three solutions showing that the change in both the value and the position decrease by a factor 4 when the mesh size and the timestep are halved.

TO: CORRESPONDING AUTHOR

AUTHOR QUERIES - TO BE ANSWERED BY THE AUTHOR

The following queries have arisen during the typesetting of your manuscript. Please answer these queries by marking the required corrections at the appropriate point in the text.

Q1	Please provide publisher, Location for reference 6, 8, 15, 17.	
Q2	Please upldate reference 10.	
Q3	Please check initial for the author "Popovici".	

Journal of Engineering Tribology

Proceedings of the Institution of Mechanical Engineers – Part   J

Offprints/Journal Order

To ensure that you receive the offprints or Journal you require please return this form with your corrections.

MS Number: JET59
Number of pages: 13
Author   Dr H C Venner

If you would prefer to receive a free copy of the Journal issue instead of 25 free offprints, please indicate below:

Quantity	I copy of the Journal issue	25 offprints
Cost	Free	Free

Please supply .... offprints/1 copy of the Journal issue* and forward to the following address:

* Delete as appropriate

Dr H C Venner
University of Twente
Faculty of Engineering Technology
P.O. Box 217
Enschede

7500 AE
The Netherlands

Quotations for additional reprints will be provided on request.